The Astrophysical Journal, 598:767–778, 2003 December 1

COBE DMR–NORMALIZED DARK ENERGY COSMOGONY

Pia Mukherjee,[1,2] A. J. Banday,[3] Alain Riazuelo,[4] Krzysztof M. Górski,[5,6] and Bharat Ratra[1]
Received 2003 June 6; accepted 2003 August 7

ABSTRACT

Likelihood analyses of the *COBE* Differential Microwave Radiometer (DMR) sky maps are used to determine the normalization of the inverse–power-law potential scalar-field dark energy model. Predictions of the DMR-normalized model are compared with various observations to constrain the allowed range of model parameters. Although the derived constraints are restrictive, evolving dark energy density scalar-field models remains an observationally viable alternative to the constant cosmological constant model.

Subject headings: cosmic microwave background — cosmology: observations — large-scale structure of universe

1. INTRODUCTION

Indications are that at the present epoch the universe is dominated by dark energy (see, e.g., Peebles & Ratra 2003 for a review and Bennett et al. 2003a for a summary of the recent *Wilkinson Microwave Anisotropy Probe* [*WMAP*] results). Einstein's cosmological constant Λ is the earliest example of dark energy, and more recently scalar-field models in which the energy density slowly decreases with time, and thus behaves like a time-variable Λ, have been the subject of much study (see, e.g., Peebles 1984; Peebles & Ratra 1988, 2003; Padmanabhan 2003).[7]

In this paper we focus on a simple dark energy scalar-field (ϕ) model. In this model the scalar-field potential energy density $V(\phi)$ at low redshift is $\propto\phi^{-\alpha}$, with $\alpha > 0$ (see, e.g., Peebles & Ratra 1988; Ratra & Peebles 1988). Consistent with the observational indications, the cosmological model is taken to be spatially flat (see, e.g., Podariu et al. 2001b; Durrer, Novosyadlyj, & Apunevych 2003; Page et al. 2003; Melchiorri & Ödman 2003).

Dark energy models, which assume an early epoch of inflation to generate the needed initial energy density fluctuations, do not predict the amplitude of these fluctuations. At present, the most robust method to fix this amplitude, and hence the normalization of the model, is to compare model predictions of the large angular scale spatial anisotropy in the cosmic microwave background (CMB) radiation with what is observed. To this end we compute the model predictions as a function of the parameter α and other cosmological parameters by following Brax, Martin, & Riazuelo (2000). We then determine the normalization amplitude by comparing these predictions with the *COBE* Differential Microwave Radiometer (DMR) CMB anisotropy measurements (Bennett et al. 1996) by following Górski et al. (1998).

In linear perturbation theory, a scalar field is mathematically equivalent to a fluid with a time-dependent equation of state parameter $w = p/\rho$ and speed of sound squared $c_s^2 = \dot{p}/\dot{\rho}$, where p is the pressure, ρ is the energy density, and the dots denote time derivatives (see, e.g., Ratra 1991). The XCDM parameterization of this dark energy model approximates w as a constant, which is accurate in the radiation- and matter-dominated epochs but not in the current, dark energy scalar-field–dominated epoch. This XCDM approximation leads to particularly inaccurate predictions for the large angular scale CMB anisotropy. We emphasize, however, that we do not work in the XCDM approximation; rather, we explicitly integrate the dark energy scalar field and other equations of motion (Brax et al. 2000).

With a robust determination of the normalization of the inverse–power-law potential dark energy scalar field, it is possible to test the model and constrain model parameter values by comparing other model predictions with observational data. In this paper we compare the predicted value, as a function of model parameters, of the rms linear mass fluctuation averaged over an 8 h^{-1} Mpc sphere,[8] $\delta M/M(8\ h^{-1}\mathrm{Mpc})$ or σ_8, with observational estimates of this quantity. We also present qualitative comparisons of the predicted fractional energy-density perturbation power spectrum $P(k)$ with various observations.

Such tests probe a combination of both the early universe physics of inflation and the late universe dark energy physics.[9] Other neoclassical cosmological tests are largely insensitive to the early universe physics of inflation and are hence more direct probes of dark energy. Of special interest are tests based on gravitational lensing (see, e.g., Ratra &

[1] Department of Physics, Kansas State University, 116 Cardwell Hall, Manhattan, KS 66506.

[2] Current address: Department of Physics and Astronomy, University of Oklahoma, 440 West Brooks Street, Norman, OK 73019.

[3] Max-Planck-Institut für Astrophysik, Karl-Schwarzschildstrasse 1, Garching D-85741, Germany.

[4] Service de Physique Théorique, CEA/DSM/SPhT, Unité de Recherche Associée au CNRS, CEA/Saclay, F-91191 Gif-sur-Yvette, Cedex, France.

[5] Jet Propulsion Laboratory, California Institute of Technology, MS 169-327, 4800 Oak Grove Drive, Pasadena, CA 91109.

[6] Warsaw University Observatory, Aleje Ujazdowskie 4, 00-478 Warsaw, Poland.

[7] Recent discussions of dark energy models include Dvali & Turner (2003), Wetterich (2003), Carroll, Hoffman, & Trodden (2003), Saini, Padmanabhan, & Bridle (2003), Jain, Dev, & Alcaniz (2003), Rosati (2003), Alam, Sahni, & Starobinsky (2003), Munshi, Porciani, & Wang (2003), Caldwell, Kamionkowski, & Weinberg (2003), Klypin et al. (2003), Silva & Bertolami (2003), Sen & Sen (2003), and Singh, Sami, & Dadhich (2003), through which the earlier literature can be accessed.

[8] Here the Hubble constant $H_0 = 100\,h$ km s^{-1} Mpc^{-1}.

[9] Another such test is the detection of the late integrated Sachs-Wolfe effect from the cross-correlation of various large-scale structure maps with maps of CMB temperature anisotropy (see Boughn & Crittenden 2003; Fosalba, Gaztañaga, & Castander 2003; Myers et al. 2003; Nolta et al. 2003; Scranton et al. 2003).

Quillen 1992; Waga & Frieman 2000; Chae et al. 2002) and Type Ia supernovae redshift–apparent magnitude (see, e.g., Podariu & Ratra 2000; Waga & Frieman 2000; Leibundgut 2001; Tonry et al. 2003) and redshift–angular size (see, e.g., Chen & Ratra 2003a; Podariu et al. 2003; Zhu & Fujimoto 2003; see also Daly & Djorgovski 2003) data.

In § 2 we summarize the techniques we use to determine the DMR estimate of the CMB rms quadrupole moment anisotropy amplitude $Q_{\text{rms-PS}}$ for the inverse–power-law potential dark energy scalar-field model. Results for $Q_{\text{rms-PS}}$ and large-scale structure statistics for the DMR-normalized models are given in § 3. These statistics are compared with current observational measurements in § 4. Our results are summarized in § 5.

2. SUMMARY OF COMPUTATION

We consider a scale-invariant primordial energy-density fluctuation power spectrum (Harrison 1970; Peebles & Yu 1970; Zel'dovich 1972), as is generated by quantum fluctuations in a weakly coupled scalar field during an early epoch of inflation (see, e.g., Fischler, Ratra, & Susskind 1985) and is consistent with the observational indications (see, e.g., Spergel et al. 2003). More precisely, the fractional energy-density perturbation power spectrum we consider is

$$P(k) = AkT^2(k) , \tag{1}$$

where k ($0 < k < \infty$) is the magnitude of the coordinate spatial wavenumber, $T(k)$ is the transfer function, and A is the normalization amplitude defined in terms of the Bardeen potential.

The CMB fractional temperature perturbation, $\delta T/T$, is expressed as a function of angular position, (θ, ϕ), on the sky via spherical harmonic decomposition:

$$\frac{\delta T}{T}(\theta,\ \phi) = \sum_{l=2}^{\infty} \sum_{m=-l}^{l} a_{lm} Y_{lm}(\theta,\ \phi) . \tag{2}$$

The CMB spatial anisotropy in a Gaussian model[10] can then be characterized by the angular perturbation spectrum C_l, defined in terms of the ensemble average,

$$\langle a_{lm} a_{l'm'}{}^{*} \rangle = C_l \delta_{ll'} \delta_{mm'} , \tag{3}$$

where the δ's are Kronecker delta functions.

The C_l's used here were computed using the Boltzmann transfer code of Brax et al. (2000). The computations here assume a standard recombination thermal history and ignore the possibility of early reionization, tilt, gravity waves, or space curvature. While observed early reionization (Bennett et al. 2003a) does affect the C_l's on the large angular scales of interest here, the effect is not large, and an accurate quantitative estimate awaits a better understanding of structure formation. At present, there is not much observational motivation for the inclusion of tilt, gravity waves, or space curvature.

[10] Simple inflation models are Gaussian, with fluctuations generated in a weakly coupled field (see, e.g., Ratra 1985; Fischler et al. 1985), consistent with observational indications (see, e.g., Mukherjee, Hobson, & Lasenby 2000; Park et al. 2001; Komatsu et al. 2002, 2003; Santos et al. 2002; De Troia et al. 2003).

The dark energy scalar-field model we consider here is characterized by the potential energy density function

$$V(\phi) = \kappa\phi^{-\alpha} , \tag{4}$$

where the constant κ has dimensions of mass raised to the power $\alpha + 4$ (Peebles & Ratra 1988). In the limit where the exponent α approaches zero, the scalar-field energy density is equivalent to a constant cosmological constant Λ. Here the exponent $\alpha \geq 0$.

We evaluate the CMB anisotropy angular spectra for a range of inverse–power-law scalar-field potential exponent α spanning the interval between 0 and 8 in steps of unity, a range of the matter density parameter Ω_0 spanning the interval between 0.1 and 1 in steps of 0.1 and for $\Omega_0 = 0.05$, and for a variety of values of the Hubble parameter h and the baryonic-mass density parameter Ω_B. The values of h were selected to cover the range of ages consistent with current requirements ($t_0 = 11$, 13, or 17 Gyr; see, e.g., Peebles & Ratra 2003), with h as a function of Ω_0 computed accordingly. The values of Ω_B were chosen to be consistent with current standard nucleosynthesis constraints ($\Omega_B h^2 =$ 0.006, 0.014, or 0.022; see, e.g., Peebles & Ratra 2003). To render the problem tractable, C_l's were determined for the central values of t_0 and $\Omega_B h^2$ and for the two combinations of these parameters that most perturb the C_l's from those computed at the central values (i.e., for the smallest t_0 we used the smallest $\Omega_B h^2$, and for the largest t_0 we used the largest $\Omega_B h^2$). Specific parameter values are given in columns (1) and (2) of Tables 1–3, and representative CMB anisotropy power spectra can be seen in Figures 1 and 2.

The differences in the low-l shapes of the C_l's in Figures 1 and 2 are a consequence of the interplay between the "usual" (fiducial CDM) Sachs-Wolfe term and the "integrated" Sachs-Wolfe term in the expression for the CMB spatial anisotropy (see, e.g., Hu & Dodelson 2002 for a review). The relative importance of these terms is determined by the values of Ω_0 and α. (These terms are not easy to estimate analytically, and we cannot trust the inaccurate XCDM approximation and must instead rely on numerical computations because these terms depend in complicated ways on the way in which w changes from its value during the matter-dominated epoch to its value at zero redshift.) More precisely, in dark energy models the gravitational potential decays with time at late time, so at late time the gravitational potential and its time derivative are of opposite sign. Consequently, there is some anticorrelation between the usual and integrated Sachs-Wolfe terms. This anticorrelation more significantly reduces the C_l's at larger Ω_0 (where the integrated term is not too large) and larger α (because the transition from matter dominance to dark energy dominance occurs earlier).

The normalizations of the theoretical CMB anisotropy spectra are determined by comparing them with the DMR data using the likelihood analysis method of Górski (1994). In this paper we utilize the DMR 4 yr co-added 53 and 90 GHz sky maps in Galactic coordinates. We do not consider the DMR ecliptic coordinates data here; the small shifts in the inferred normalization amplitudes due to the small differences in the Galactic- and ecliptic-coordinate maps are quantified in Górski et al. (1998). The 53 and 90 GHz maps are co-added using inverse noise variance weights. The main changes relative to the analysis of Górski et al. (1998) are that we use the DMR maps in the HEALPix

TABLE 1

$Q_{\text{rms-PS}}$ VALUES FOR THE $t_0 = 13$ Gyr, $\Omega_B h^2 = 0.014$ MODELS

		$Q_{\text{rms-PS}}$ (μK)							
		$\alpha = 0$		$\alpha = 2$		$\alpha = 4$		$\alpha = 6$	
Ω_0 (1)	h (2)	Correction,[a] $l_{\min} = 2$ (3)	No Correction,[a] $l_{\min} = 3$ (4)	Correction, $l_{\min} = 2$ (5)	No Correction, $l_{\min} = 3$ (6)	Correction, $l_{\min} = 2$ (7)	No Correction, $l_{\min} = 3$ (8)	Correction, $l_{\min} = 2$ (9)	No Correction, $l_{\min} = 3$ (10)
0.1	0.96	$22.52^{24.12\ 25.84}_{21.00\ 19.56}$	$23.88^{25.52\ 27.36}_{22.28\ 20.80}$	$24.76^{26.60\ 28.56}_{23.04\ 21.40}$	$26.36^{28.24\ 30.28}_{24.56\ 22.84}$	$26.68^{28.68\ 30.80}_{24.84\ 23.08}$	$28.44^{30.48\ 32.64}_{26.52\ 24.64}$	$28.44^{30.52\ 32.76}_{26.44\ 24.56}$	$30.32^{32.36\ 34.64}_{28.20\ 26.24}$
0.2	0.81	$20.20^{21.60\ 23.12}_{18.84\ 17.56}$	$21.36^{22.88\ 24.40}_{19.96\ 18.64}$	$22.52^{24.12\ 25.92}_{20.96\ 19.52}$	$23.88^{25.56\ 27.40}_{22.28\ 20.80}$	$24.32^{26.12\ 28.04}_{22.68\ 21.04}$	$25.84^{27.72\ 29.72}_{24.12\ 22.48}$	$25.76^{27.64\ 29.68}_{23.96\ 22.24}$	$27.40^{29.32\ 31.44}_{25.52\ 23.76}$
0.3	0.72	$18.80^{20.08\ 21.48}_{17.56\ 16.36}$	$19.84^{21.20\ 22.64}_{18.60\ 17.36}$	$20.56^{22.04\ 23.60}_{19.20\ 17.88}$	$21.76^{23.28\ 24.92}_{20.36\ 19.00}$	$22.20^{23.80\ 25.56}_{20.72\ 19.28}$	$23.56^{25.20\ 27.00}_{22.00\ 20.52}$	$23.44^{25.12\ 26.96}_{21.84\ 20.32}$	$24.88^{26.60\ 28.52}_{23.20\ 21.64}$
0.4	0.67	$17.96^{19.20\ 20.52}_{16.80\ 15.68}$	$18.96^{20.24\ 21.60}_{17.76\ 16.60}$	$18.84^{20.16\ 21.60}_{17.60\ 16.44}$	$19.92^{21.28\ 22.76}_{18.64\ 17.44}$	$20.16^{21.56\ 23.12}_{18.84\ 17.56}$	$21.32^{22.80\ 24.40}_{19.96\ 18.64}$	$21.16^{22.68\ 24.28}_{19.76\ 18.40}$	$22.40^{23.96\ 25.64}_{20.96\ 19.56}$
0.5	0.62	$17.40^{18.60\ 19.88}_{16.28\ 15.24}$	$18.36^{19.60\ 20.92}_{17.24\ 16.08}$	$17.52^{18.72\ 20.00}_{16.40\ 15.32}$	$18.48^{19.72\ 21.08}_{17.32\ 16.20}$	$18.20^{19.44\ 20.80}_{17.00\ 15.88}$	$19.20^{20.52\ 21.92}_{18.00\ 16.80}$	$18.92^{20.20\ 21.64}_{17.68\ 16.52}$	$20.00^{21.36\ 22.80}_{18.72\ 17.48}$
0.6	0.59	$17.12^{18.28\ 19.52}_{16.04\ 15.00}$	$18.04^{19.24\ 20.56}_{16.92\ 15.84}$	$16.48^{17.60\ 18.84}_{15.44\ 14.44}$	$17.40^{18.52\ 19.80}_{16.28\ 15.24}$	$16.52^{17.64\ 18.84}_{15.48\ 14.44}$	$17.40^{18.56\ 19.84}_{16.32\ 15.28}$	$16.80^{17.92\ 19.16}_{15.72\ 14.68}$	$17.68^{18.88\ 20.12}_{16.60\ 15.52}$
0.7	0.56	$16.96^{18.12\ 19.36}_{15.88\ 14.84}$	$17.88^{19.08\ 20.36}_{16.76\ 15.68}$	$15.96^{17.00\ 18.20}_{14.92\ 13.96}$	$16.80^{17.92\ 19.08}_{15.76\ 14.76}$	$15.44^{16.48\ 17.60}_{14.48\ 13.52}$	$16.24^{17.32\ 18.48}_{15.24\ 14.28}$	$15.16^{16.16\ 17.24}_{14.20\ 13.28}$	$15.92^{16.96\ 18.12}_{14.96\ 14.00}$
0.8	0.54	$16.96^{18.08\ 19.32}_{15.84\ 14.80}$	$17.88^{19.04\ 20.32}_{16.72\ 15.68}$	$15.88^{16.96\ 18.08}_{14.88\ 13.88}$	$16.72^{17.80\ 19.00}_{15.68\ 14.68}$	$15.08^{16.08\ 17.16}_{14.12\ 13.20}$	$15.88^{16.88\ 18.04}_{14.88\ 13.96}$	$14.48^{15.44\ 16.48}_{13.60\ 12.72}$	$15.24^{16.24\ 17.32}_{14.32\ 13.40}$
0.9	0.52	$16.96^{18.12\ 19.36}_{15.88\ 14.84}$	$17.92^{19.08\ 20.36}_{16.76\ 15.72}$	$16.32^{17.40\ 18.60}_{15.28\ 14.28}$	$17.16^{18.32\ 19.56}_{16.12\ 15.08}$	$15.64^{16.72\ 17.84}_{14.68\ 13.72}$	$16.48^{17.56\ 18.72}_{15.48\ 14.48}$	$15.24^{16.24\ 17.32}_{14.28\ 13.32}$	$16.00^{17.08\ 18.20}_{15.04\ 14.08}$
1	0.50	$17.04^{18.20\ 19.48}_{15.96\ 14.92}$	$18.00^{19.20\ 20.48}_{16.88\ 15.76}$	$17.08^{18.24\ 19.52}_{16.00\ 14.96}$	$18.04^{19.20\ 20.52}_{16.92\ 15.80}$	$17.04^{18.20\ 19.44}_{15.96\ 14.88}$	$17.96^{19.16\ 20.44}_{16.84\ 15.76}$	$17.04^{18.20\ 19.48}_{15.96\ 14.92}$	$18.00^{19.20\ 20.48}_{16.88\ 15.76}$

NOTES.—The tabulated $Q_{\text{rms-PS}}$ values are determined from the conditional likelihood function at fixed Ω_0 and α. At each Ω_0 and α, the first of the five entries in each of cols. (3)–(10) is the maximum likelihood value, the first (vertical) pair delimits the 68.3% (1 σ) highest posterior density range, and the second (vertical) pair delimits the 95.5% (2 σ) highest posterior density range.

[a] Accounting for or ignoring the correction for faint high-latitude foreground Galactic emission.

pixelization and excise pixels likely to be contaminated by bright foreground emission on and near the Galactic plane (Banday et al. 1997) using a cut rederived from the DIRBE 140 μm data. The DIRBE map was reconstructed in the HEALPix format using the publicly available Calibrated Individual Observations files together with the DIRBE Sky and Zodi Atlas (both products are described in Hauser et al. 1998), allowing the construction of a full-sky map corrected for the zodiacal emission according to the model of Kelsall et al. (1998). We consider C_l's to multipole $l \leq 30$. See Górski et al. (1998) for a more detailed description of the method.

As mentioned, we excise sky-map pixels on and near the Galactic plane where foreground emission dominates the CMB. Following Górski et al. (1998; see also Górski et al. 1995, 1996) we quantify the extent to which residual high-latitude Galactic emission can modify our results in two ways: by performing all computations both including and excluding the observed sky quadrupole and by performing all computations with and without correcting for emission correlated with the DIRBE 140 μm sky map, itself fitted to the data for each model.[11]

3. RESULTS

3.1. *Results of $Q_{rms\text{-}PS}$ Fitting*

The results of the DMR likelihood analysis are summarized in Figures 3–9 and Tables 1–3. We have computed

[11] See Górski et al. (1998) for a more detailed discussion. More recent discussions of foreground emissions can be accessed through Mukherjee et al. (2002, 2003a), Banday et al. (2003), and Bennett et al. (2003b).

TABLE 2

$Q_{\text{rms-PS}}$ VALUES FOR THE $t_0 = 11$ Gyr, $\Omega_B h^2 = 0.006$ MODELS

		$Q_{\text{rms-PS}}$ (μK)							
		$\alpha = 0$		$\alpha = 2$		$\alpha = 4$		$\alpha = 6$	
Ω_0 (1)	h (2)	Correction,[a] $l_{\min} = 2$ (3)	No Correction,[a] $l_{\min} = 3$ (4)	Correction, $l_{\min} = 2$ (5)	No Correction, $l_{\min} = 3$ (6)	Correction, $l_{\min} = 2$ (7)	No Correction, $l_{\min} = 3$ (8)	Correction, $l_{\min} = 2$ (9)	No Correction, $l_{\min} = 3$ (10)
0.1	1.13	$22.72^{24.36\ 26.12}_{21.16\ 19.68}$	$24.12^{25.80\ 27.64}_{22.52\ 20.96}$	$24.96^{26.84\ 28.84}_{23.24\ 21.56}$	$25.96^{28.52\ 30.60}_{24.76\ 23.04}$	$26.96^{28.96\ 31.16}_{25.04\ 23.24}$	$28.72^{30.80\ 32.96}_{26.76\ 24.84}$	$28.76^{30.92\ 33.16}_{26.76\ 24.80}$	$30.64^{32.76\ 35.12}_{28.56\ 26.52}$
0.2	0.96	$20.36^{21.80\ 23.36}_{19.00\ 17.72}$	$21.56^{23.04\ 24.68}_{20.16\ 18.84}$	$22.68^{24.32\ 26.12}_{21.12\ 19.64}$	$24.08^{25.80\ 27.64}_{22.48\ 20.92}$	$24.56^{26.36\ 28.32}_{22.84\ 21.24}$	$26.12^{27.96\ 30.00}_{24.32\ 22.64}$	$26.00^{27.96\ 30.04}_{24.20\ 22.48}$	$27.68^{29.68\ 31.84}_{25.80\ 24.04}$
0.3	0.86	$18.96^{20.28\ 21.72}_{17.72\ 16.52}$	$20.04^{21.40\ 22.88}_{18.76\ 17.56}$	$20.76^{22.24\ 23.84}_{19.36\ 18.04}$	$22.00^{23.52\ 25.16}_{20.56\ 19.16}$	$22.44^{24.04\ 25.80}_{20.88\ 19.44}$	$23.80^{25.48\ 27.28}_{22.24\ 20.68}$	$23.64^{25.36\ 27.24}_{22.04\ 20.48}$	$25.12^{26.88\ 28.84}_{23.48\ 21.84}$
0.4	0.79	$18.12^{19.36\ 20.72}_{16.92\ 15.80}$	$19.12^{20.44\ 21.84}_{17.92\ 16.76}$	$19.04^{20.36\ 21.80}_{17.76\ 16.56}$	$20.12^{21.52\ 23.04}_{18.84\ 17.60}$	$20.36^{21.80\ 23.32}_{19.00\ 17.68}$	$21.52^{23.04\ 24.64}_{20.16\ 18.80}$	$21.36^{22.88\ 24.52}_{19.96\ 18.56}$	$22.64^{24.20\ 25.92}_{21.16\ 19.76}$
0.5	0.74	$17.60^{18.80\ 20.12}_{16.48\ 15.36}$	$18.56^{19.80\ 21.16}_{17.40\ 16.24}$	$17.68^{18.88\ 20.24}_{16.52\ 15.44}$	$18.68^{19.92\ 21.28}_{17.48\ 16.32}$	$18.36^{19.64\ 21.00}_{17.16\ 16.04}$	$19.40^{20.72\ 22.16}_{18.16\ 16.96}$	$19.12^{20.44\ 21.88}_{17.88\ 16.64}$	$20.20^{21.60\ 23.08}_{18.92\ 17.68}$
0.6	0.70	$17.28^{18.44\ 19.72}_{16.16\ 15.08}$	$18.24^{19.44\ 20.76}_{17.08\ 15.96}$	$16.60^{17.76\ 19.00}_{15.56\ 14.52}$	$17.52^{18.72\ 20.00}_{16.44\ 15.36}$	$16.68^{17.80\ 19.04}_{15.60\ 14.56}$	$17.60^{18.76\ 20.04}_{16.48\ 15.40}$	$16.96^{18.12\ 19.36}_{15.88\ 14.84}$	$17.88^{19.08\ 20.36}_{16.76\ 15.68}$
0.7	0.66	$17.12^{18.24\ 19.56}_{16.00\ 14.96}$	$18.04^{19.24\ 20.56}_{16.92\ 15.80}$	$16.08^{17.20\ 18.36}_{15.08\ 14.04}$	$16.96^{18.08\ 19.32}_{15.88\ 14.88}$	$15.60^{16.64\ 17.76}_{14.60\ 13.64}$	$16.40^{17.48\ 18.68}_{15.36\ 14.40}$	$15.28^{16.32\ 17.44}_{14.32\ 13.40}$	$16.08^{17.16\ 18.28}_{15.12\ 14.12}$
0.8	0.64	$17.08^{18.24\ 19.48}_{16.00\ 14.92}$	$18.00^{19.20\ 20.52}_{16.88\ 15.80}$	$16.04^{17.12\ 18.28}_{15.00\ 14.00}$	$16.88^{18.00\ 19.20}_{15.84\ 14.80}$	$15.24^{16.24\ 17.36}_{14.24\ 13.32}$	$16.00^{17.08\ 18.20}_{15.04\ 14.04}$	$14.64^{15.60\ 16.68}_{13.72\ 12.84}$	$15.40^{16.40\ 17.48}_{14.44\ 13.52}$
0.9	0.61	$17.12^{18.32\ 19.56}_{16.04\ 15.00}$	$18.08^{19.28\ 20.60}_{16.92\ 15.84}$	$16.44^{17.56\ 18.76}_{15.40\ 14.36}$	$17.32^{18.48\ 19.72}_{16.24\ 15.20}$	$15.80^{16.88\ 18.00}_{14.80\ 13.80}$	$16.64^{17.72\ 18.92}_{15.60\ 14.60}$	$15.36^{16.40\ 17.48}_{14.40\ 13.44}$	$16.16^{17.20\ 18.40}_{15.16\ 14.20}$
1	0.59	$17.20^{18.40\ 19.64}_{16.12\ 15.04}$	$18.16^{19.36\ 20.68}_{17.00\ 15.92}$	$17.24^{18.40\ 19.68}_{16.12\ 15.04}$	$18.20^{19.40\ 20.72}_{17.04\ 15.96}$	$17.16^{18.36\ 19.60}_{16.08\ 15.00}$	$18.12^{19.32\ 20.64}_{16.96\ 15.88}$	$17.20^{18.40\ 19.64}_{16.12\ 15.04}$	$18.16^{19.36\ 20.68}_{17.00\ 15.92}$

NOTES.—The tabulated $Q_{\text{rms-PS}}$ values are determined from the conditional likelihood function at fixed Ω_0 and α. At each Ω_0 and α, the first of the five entries in each of cols. (3)–(10) is the maximum likelihood value, the first (vertical) pair delimits the 68.3% (1 σ) highest posterior density range, and the second (vertical) pair delimits the 95.5% (2 σ) highest posterior density range.

[a] Accounting for or ignoring the correction for faint high-latitude foreground Galactic emission.

TABLE 3

$Q_{\text{rms-PS}}$ VALUES FOR THE $t_0 = 17$ Gyr, $\Omega_B h^2 = 0.022$ MODELS

		$Q_{\text{rms-PS}}$ (μK)							
		$\alpha = 0$		$\alpha = 2$		$\alpha = 4$		$\alpha = 6$	
Ω_0 (1)	h (2)	Correction,[a] $l_{\min} = 2$ (3)	No Correction,[a] $l_{\min} = 3$ (4)	Correction, $l_{\min} = 2$ (5)	No Correction, $l_{\min} = 3$ (6)	Correction, $l_{\min} = 2$ (7)	No Correction, $l_{\min} = 3$ (8)	Correction, $l_{\min} = 2$ (9)	No Correction, $l_{\min} = 3$ (10)
0.1	0.73	$22.20^{23.76\ 25.44}_{20.72\ 19.28}$	$23.52^{25.12\ 26.88}_{21.96\ 20.52}$	$24.48^{26.28\ 28.20}_{22.80\ 21.20}$	$26.00^{27.88\ 29.84}_{24.28\ 22.60}$	$26.24^{28.20\ 30.28}_{24.44\ 22.72}$	$27.92^{29.92\ 32.04}_{26.04\ 24.28}$	$27.84^{29.92\ 32.08}_{25.92\ 24.08}$	$29.68^{31.72\ 33.88}_{27.68\ 25.76}$
0.2	0.62	$19.88^{21.24\ 22.76}_{18.56\ 17.32}$	$21.00^{22.44\ 23.96}_{19.68\ 18.40}$	$22.28^{23.84\ 25.60}_{20.76\ 19.32}$	$23.60^{25.24\ 27.04}_{22.04\ 20.56}$	$24.04^{25.08\ 27.68}_{22.40\ 20.84}$	$25.56^{27.36\ 29.28}_{23.84\ 22.24}$	$25.36^{27.20\ 29.20}_{23.60\ 21.96}$	$26.96^{28.88\ 30.92}_{25.16\ 23.44}$
0.3	0.55	$18.60^{19.88\ 21.24}_{17.40\ 16.24}$	$19.64^{20.96\ 22.40}_{18.40\ 17.20}$	$20.36^{21.76\ 23.36}_{19.00\ 17.72}$	$21.56^{23.04\ 24.60}_{20.16\ 18.80}$	$21.96^{23.52\ 25.24}_{20.48\ 19.08}$	$23.28^{24.92\ 26.64}_{21.76\ 20.28}$	$23.08^{24.76\ 26.52}_{21.56\ 20.04}$	$24.52^{26.20\ 28.08}_{22.88\ 21.36}$
0.4	0.51	$17.76^{19.00\ 20.28}_{16.64\ 15.52}$	$18.76^{20.00\ 21.36}_{17.56\ 16.44}$	$18.68^{20.00\ 21.36}_{17.48\ 16.28}$	$19.76^{21.08\ 22.52}_{18.48\ 17.28}$	$19.92^{21.32\ 22.84}_{18.64\ 17.36}$	$21.08^{22.52\ 24.08}_{19.72\ 18.44}$	$20.88^{22.36\ 23.92}_{19.52\ 18.16}$	$22.12^{23.60\ 25.24}_{20.68\ 19.28}$
0.5	0.48	$17.20^{18.36\ 19.64}_{16.12\ 15.04}$	$18.16^{19.36\ 20.64}_{17.04\ 15.92}$	$17.32^{18.48\ 19.76}_{16.20\ 15.12}$	$18.24^{19.48\ 20.80}_{17.12\ 16.00}$	$18.00^{19.24\ 20.56}_{16.84\ 15.72}$	$19.00^{20.28\ 21.64}_{17.80\ 16.64}$	$18.68^{19.92\ 21.32}_{17.48\ 16.28}$	$19.72^{21.04\ 22.44}_{18.48\ 17.28}$
0.6	0.45	$16.96^{18.12\ 19.36}_{15.92\ 14.88}$	$17.88^{19.08\ 20.36}_{16.80\ 15.72}$	$16.32^{17.40\ 18.60}_{15.28\ 14.28}$	$17.20^{18.32\ 19.56}_{16.12\ 15.08}$	$16.36^{17.44\ 18.68}_{15.32\ 14.32}$	$17.24^{18.36\ 19.60}_{16.16\ 15.12}$	$16.56^{17.68\ 18.92}_{15.52\ 14.52}$	$17.48^{18.60\ 19.84}_{16.36\ 15.32}$
0.7	0.43	$16.76^{17.92\ 19.12}_{15.72\ 14.68}$	$17.68^{18.84\ 20.12}_{16.56\ 15.52}$	$15.80^{16.88\ 18.04}_{14.84\ 13.84}$	$16.64^{17.76\ 18.92}_{15.64\ 14.60}$	$15.28^{16.28\ 17.36}_{14.32\ 13.36}$	$16.04^{17.08\ 18.24}_{15.04\ 14.12}$	$14.96^{15.92\ 17.00}_{14.00\ 13.12}$	$15.72^{16.72\ 17.84}_{14.76\ 13.80}$
0.8	0.41	$16.80^{17.92\ 19.12}_{15.72\ 14.68}$	$17.68^{18.84\ 20.12}_{16.60\ 15.52}$	$15.72^{16.80\ 17.92}_{14.76\ 13.76}$	$16.56^{17.64\ 18.84}_{15.52\ 14.56}$	$14.96^{15.96\ 17.04}_{14.04\ 13.12}$	$15.72^{16.76\ 17.88}_{14.76\ 13.84}$	$14.32^{15.28\ 16.28}_{13.44\ 12.60}$	$15.08^{16.04\ 17.08}_{14.16\ 13.24}$
0.9	0.40	$16.84^{17.96\ 19.20}_{15.76\ 14.72}$	$17.76^{18.92\ 20.16}_{16.64\ 15.56}$	$16.16^{17.24\ 18.44}_{15.16\ 14.16}$	$17.00^{18.12\ 19.36}_{15.96\ 14.96}$	$15.52^{16.56\ 17.68}_{14.56\ 13.60}$	$16.36^{17.40\ 18.56}_{15.32\ 14.36}$	$15.04^{16.00\ 17.08}_{14.08\ 13.16}$	$15.80^{16.84\ 17.92}_{14.84\ 13.88}$
1	0.38	$16.84^{18.04\ 19.28}_{15.84\ 14.80}$	$17.84^{19.00\ 20.28}_{16.72\ 15.64}$	$16.92^{18.08\ 19.32}_{15.88\ 14.84}$	$17.84^{19.00\ 20.28}_{16.72\ 15.64}$	$16.92^{18.04\ 19.28}_{15.84\ 14.80}$	$17.80^{19.00\ 20.28}_{16.72\ 15.64}$	$16.92^{18.08\ 19.32}_{15.88\ 14.84}$	$17.84^{19.04\ 20.32}_{16.76\ 15.68}$

NOTES.—The tabulated $Q_{\text{rms-PS}}$ values are determined from the conditional likelihood function at fixed Ω_0 and α. At each Ω_0 and α, the first of the five entries in each of cols. (3)–(10) is the maximum likelihood value, the first (vertical) pair delimits the 68.3% (1 σ) highest posterior density range, and the second (vertical) pair delimits the 95.5% (2 σ) highest posterior density range.

[a] Accounting for or ignoring the correction for faint high-latitude foreground Galactic emission.

DMR data likelihood functions $L(Q_{\text{rms-PS}}, \Omega_0, \alpha)$ using three sets of C_l's computed for values of $(\Omega_B h^2, t_0) =$ (0.014, 13 Gyr), (0.006, 11 Gyr), and (0.022, 17 Gyr). We have also considered four "different" DMR data sets, either accounting for or ignoring the correction for faint high-latitude foreground Galactic emission and either including or excluding the quadrupole moment from the analysis.

Variations in Ω_0 and α have the largest effect on the inferred value of $Q_{\text{rms-PS}}$ from the DMR data. Changes in $\Omega_B h^2$, t_0, faint high-latitude Galactic emission treatment, and quadrupole moment treatment have much smaller effects, consistent with the findings of Górski et al. (1998). These results determine what we have chosen to display in Figures 3–9 and Tables 1–3.

Two representative sets of likelihood functions $L(Q_{\text{rms-PS}}, \Omega_0)$ are shown in Figures 3 and 4. Figure 3 shows those derived while accounting for the correction for faint high-latitude foreground Galactic emission and including the quadrupole moment in the analysis. Figure 4 shows the likelihood functions derived while ignoring the faint high-latitude foreground Galactic emission correction and excluding the quadrupole moment from the analysis. These data sets represent two different ways of dealing with the effects of foreground emission on the inferred $Q_{\text{rms-PS}}$ normalization (with the former resulting in a typically 5% lower $Q_{\text{rms-PS}}$ value). These two data sets span the range of normalizations inferred from our analysis here.[12] The other two data sets we have used here, accounting for the faint high-latitude foreground emission while excluding the quadrupole and not accounting for the faint high-latitude foreground emission while including the quadrupole, result in $Q_{\text{rms-PS}}$ normalizations that are typically 1%–2% above the smaller value or below the larger value of the first two data sets.

[12] The ecliptic-frame sky maps result in slightly larger inferred $Q_{\text{rms-PS}}$ normalization values than the Galactic-frame sky maps used here; see Górski et al. (1998).

Tables 1–3 give the $Q_{\text{rms-PS}}$ central values and 1 and 2 σ ranges, computed from the appropriate posterior probability density distribution function assuming a uniform prior. These tables are computed for the three cases with $\Omega_B h^2 = 0.014$ and $t_0 = 13$ Gyr (Table 1), $\Omega_B h^2 = 0.006$ and $t_0 = 11$ Gyr (Table 2), and $\Omega_B h^2 = 0.022$ and $t_0 = 17$ Gyr (Table 3). We present results for four representative values of α (=0, 2, 4, and 6) and a range of values of Ω_0 spanning the interval from 0.1 to 1. The $Q_{\text{rms-PS}}$ values are given only for the two extreme data sets, whose likelihood functions are shown in Figures 3 and 4: the faint high-latitude Galactic foreground emission–corrected, quadrupole-included case and the Galactic foreground emission–uncorrected, quadrupole-excluded case.

Figure 5 shows the ridge lines of the maximum likelihood $Q_{\text{rms-PS}}$ value as a function of Ω_0, for two different values of α, for all four data sets used in this paper. Figures 7*a* and 7*c* show the effect the small differences between data sets have on the conditional (fixed Ω_0, α, $\Omega_B h^2$, and t_0) likelihood function for $Q_{\text{rms-PS}}$.

Tables 1–3 also illustrate the shift in the inferred $Q_{\text{rms-PS}}$ normalization amplitudes due to changes in t_0 and $\Omega_B h^2$. Figure 6 shows the effects that varying t_0 and $\Omega_B h^2$ have on the ridge lines of the maximum likelihood $Q_{\text{rms-PS}}$ as a function of Ω_0. Figures 7*b* and 7*d* show the effects of varying t_0 and $\Omega_B h^2$ on the conditional (fixed Ω_0 and α) likelihood functions for $Q_{\text{rms-PS}}$ for a given data set. On the whole, for the CMB anisotropy spectra considered here, shifts in t_0 and $\Omega_B h^2$ have only a small effect on the inferred normalization amplitude.

Future *WMAP* data (see, e.g., Bennett et al. 2003a) should be able to significantly constrain the dark energy scalar-field model. Here we use the DMR-normalized dark energy model predictions to semiquantitatively constrain the cosmological parameters of this model. Since we do not attempt to determine precise constraints on these parameters in this paper, we do not combine results from analyses of all DMR data sets, as Górski et al. (1998) did for the open model (Gott 1982; Ratra & Peebles 1995), to deter-

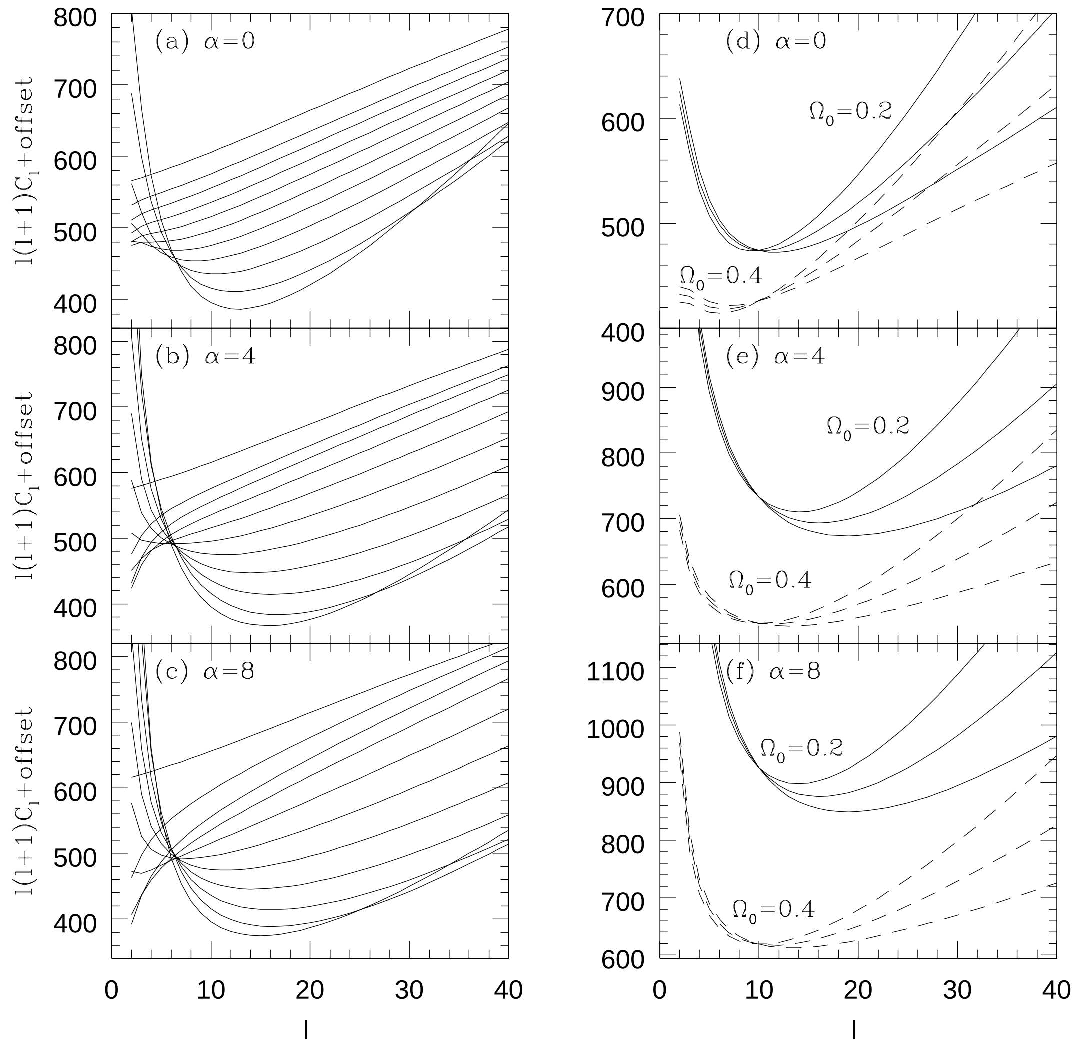

FIG. 1.—CMB anisotropy multipole coefficients. Panels *a* and *d*, *b* and *e*, and *c* and *f* correspond to models with $\alpha = 0$, 4, and 8, respectively. (*a*)–(*c*) Multipoles for a model with $t_0 = 13$ Gyr and $\Omega_B h^2 = 0.014$. The coefficients are normalized relative to the C_9 amplitude, and different values of Ω_0 are offset from each other to aid visualization. In each of these panels, at $l = 9$, the 11 curves in ascending order correspond to models with $\Omega_0 = 0.05, 0.1, 0.2, \ldots,$ 0.9, and 1.0. (*d*)–(*f*) Models with $\Omega_0 = 0.2$ (*solid curves*) and 0.4 (*dashed curves*). Each set of three curves in these panels corresponds, in ascending order on the right vertical axis of each panel, to models with parameter values $(t_0,\ \Omega_B h^2) = (11$ Gyr, $0.006)$, (13 Gyr, 0.014), and (17 Gyr, 0.022), respectively.

mine the most robust estimate of the $Q_{\text{rms-PS}}$ normalization amplitudes.

Figures 8 and 9 show marginal likelihood functions for some of the cosmological model parameter values and DMR data sets considered here. Figure 8 shows the likelihood function $L(\Omega_0,\ \alpha)$ derived by marginalizing $L(\Omega_0,\ \alpha,\ Q_{\text{rms-PS}})$ over $Q_{\text{rms-PS}}$ with a uniform prior. Figure 9 shows conditional (on slices of constant α or Ω_0) projections of the two-dimensional likelihood functions of Figure 8. The effects of Galactic foreground correction and inclusion of the quadrupole are important. While the DMR data qualitatively indicate that lower α and higher Ω_0 values are mildly favored, these data by themselves do not provide significant quantitative constraints on cosmological model parameter values.

3.2. *Computation of Large-Scale Structure Statistics*

The fractional energy-density perturbation power spectrum $P(k)$ (eq. [1]) was evaluated from a numerical integration of the linear perturbation theory equations of motion. Table 4 lists the $P(k)$ normalization amplitudes A (eq. [1]) for a range of Ω_0 and α values.[13] The normalization amplitude is quite insensitive to the values of $\Omega_B h^2$ and t_0 used. It is more sensitive to the choice of DMR data set, and Figure 10 shows representative $P(k)$'s normalized to $Q_{\text{rms-PS}}$ obtained by averaging those from the foreground-emission–corrected quadrupole-included analysis and the foreground-emission–uncorrected quadrupole-excluded analysis. Figure 10 also shows recent observational determinations of the galaxy power spectrum on linear scales. The predicted matter power spectrum $P(k) \propto (Q_{\text{rms-PS}})^2$, so the error in the DMR normalization of $P(k)$ is approximately twice that in the DMR determination of $Q_{\text{rms-PS}}$ (which is discussed below). As always, when comparing model predictions with observational measurements, it is important to account for this normalization uncertainty, rather than basing conclusions about model viability solely on the "central" normalization value.

[13] Numerical noise and other small effects contribute to the tiny artificial differences between the various $\Omega_0 = 1$ model predictions in this and other tables.

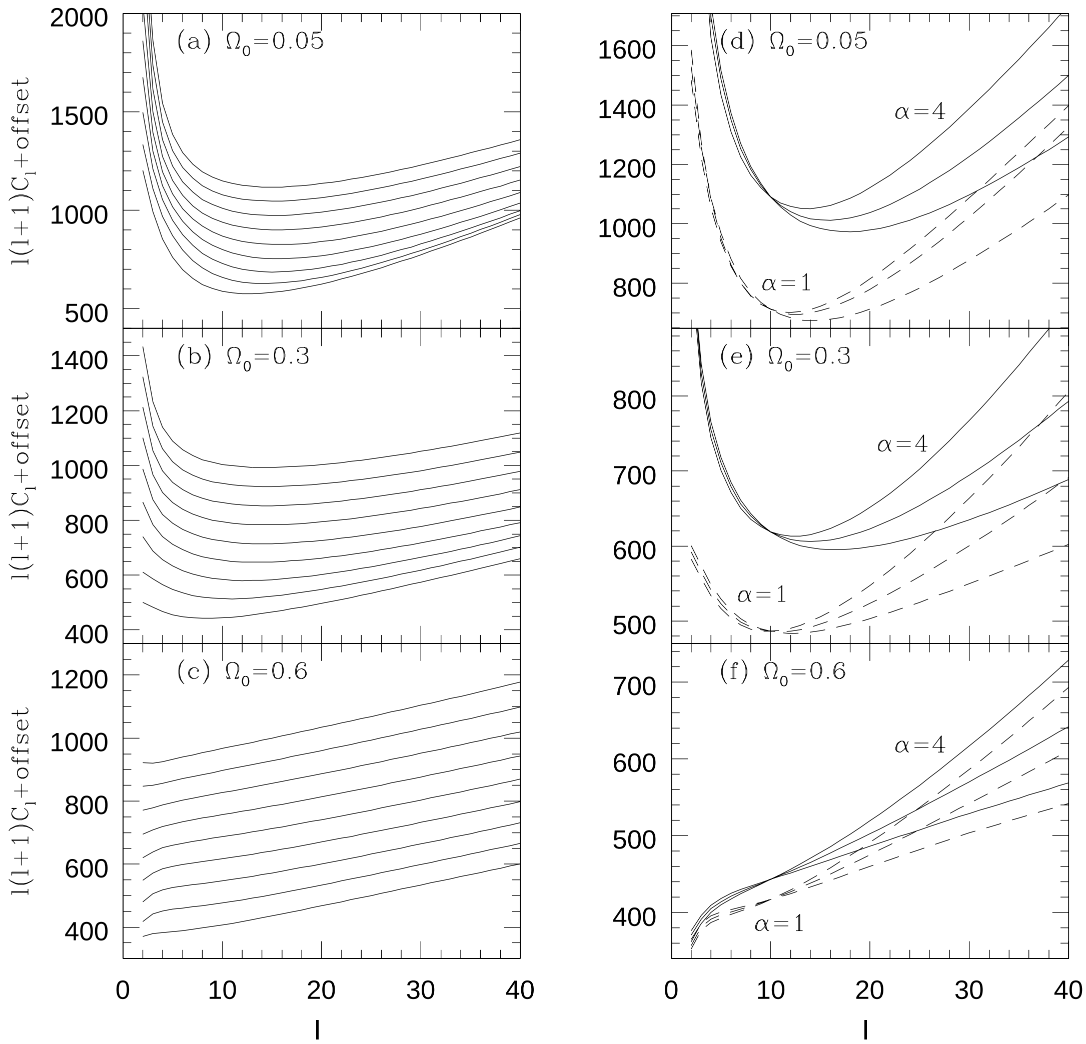

FIG. 2.—CMB anisotropy multipole coefficients. Panels *a* and *d*, *b* and *e*, and *c* and *f* correspond to models with $\Omega_0 = 0.05$, 0.3, and 0.6, respectively. (*a*)–(*c*) Multipoles for a model with $t_0 = 13$ Gyr and $\Omega_B h^2 = 0.014$. The coefficients are normalized relative to the C_9 amplitude, and different values of α are offset from each other to aid visualization. In each of these panels, at $l = 9$, the nine curves in ascending order correspond to models with $\alpha = 0, 1, 2, \ldots, 7$, and 8. (*d*)–(*f*) Models with $\alpha = 4$ (*solid curves*) and 1 (*dashed curves*). Each set of three curves in these panels corresponds, in ascending order on the right vertical axis of each panel, to models with parameter values $(t_0,\ \Omega_B h^2) = (11\ \text{Gyr},\ 0.006)$, (13 Gyr, 0.014), and (17 Gyr, 0.022), respectively.

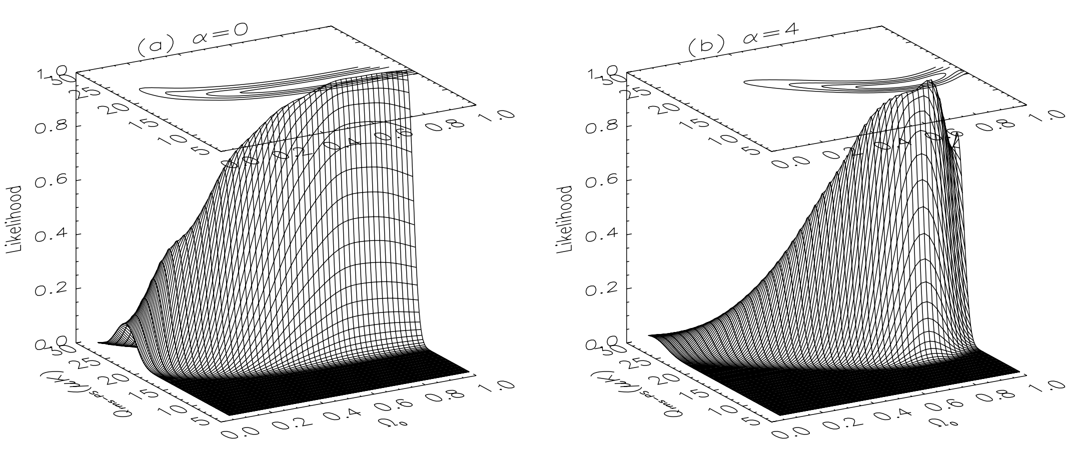

FIG. 3.—Likelihood functions $L(Q_{\text{rms-PS}},\ \Omega_0)$ (arbitrarily normalized to unity at the highest peak) derived from a simultaneous analysis of the DMR 53 and 90 GHz Galactic-frame data, corrected for faint high-latitude foreground Galactic emission and including the quadrupole moment in the analysis. These are for the model with $t_0 = 13$ Gyr and $\Omega_B h^2 = 0.014$. (*a*) For $\alpha = 0$. (*b*) For $\alpha = 4$.

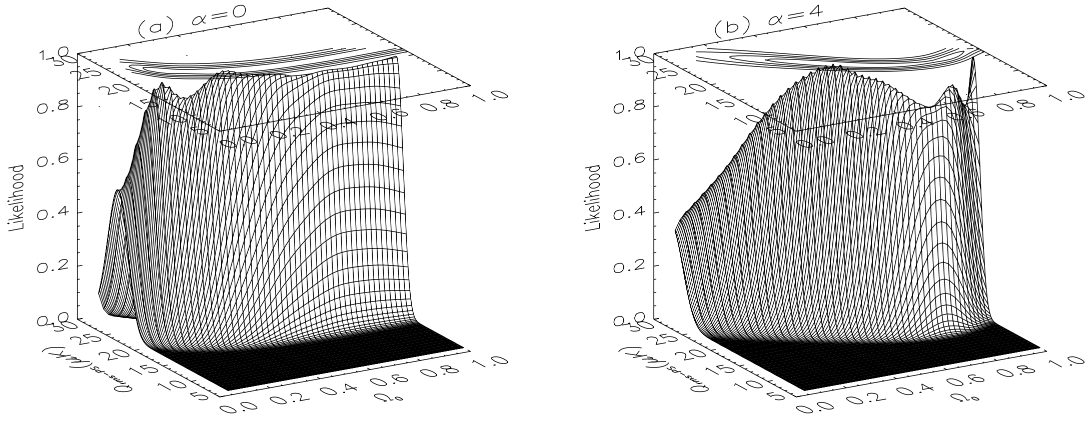

FIG. 4.—Likelihood functions $L(Q_{\text{rms-PS}},\ \Omega_0)$ (arbitrarily normalized to unity at the highest peak) derived from a simultaneous analysis of the DMR 53 and 90 GHz Galactic-frame data, ignoring the correction for faint high-latitude foreground Galactic emission and excluding the quadrupole moment from the analysis. These are for the model with $t_0 = 13$ Gyr and $\Omega_B h^2 = 0.014$. (*a*) For $\alpha = 0$. (*b*) For $\alpha = 4$.

The mean square linear mass fluctuation averaged over a sphere of coordinate radius $\bar{\chi}$ is

$$\left\langle \left[\frac{\delta M}{M}(\bar{\chi})\right]^2 \right\rangle = \frac{9}{2\pi^2}\int_0^\infty dk\, \frac{k^2 P(k)}{(k\bar{\chi})^6}\left[\sin(k\bar{\chi}) - k\bar{\chi}\cos(k\bar{\chi})\right]^2 . \quad (5)$$

Tables 5–7 list predictions for $(\delta M/M)(8\ h^{-1}\ \text{Mpc})$ or σ_8, the square root of the above expression evaluated at 8 h^{-1} Mpc, for various values of α and Ω_0. In Tables 5–7 we list the mean of the central values obtained from the foreground-emission–corrected quadrupole-included analysis and the foreground-emission–uncorrected quadrupole-excluded analysis.

Górski et al. (1998) show that the maximal 1 σ fractional $Q_{\text{rms-PS}}$ (and hence $\delta M/M$) uncertainty from the DMR data

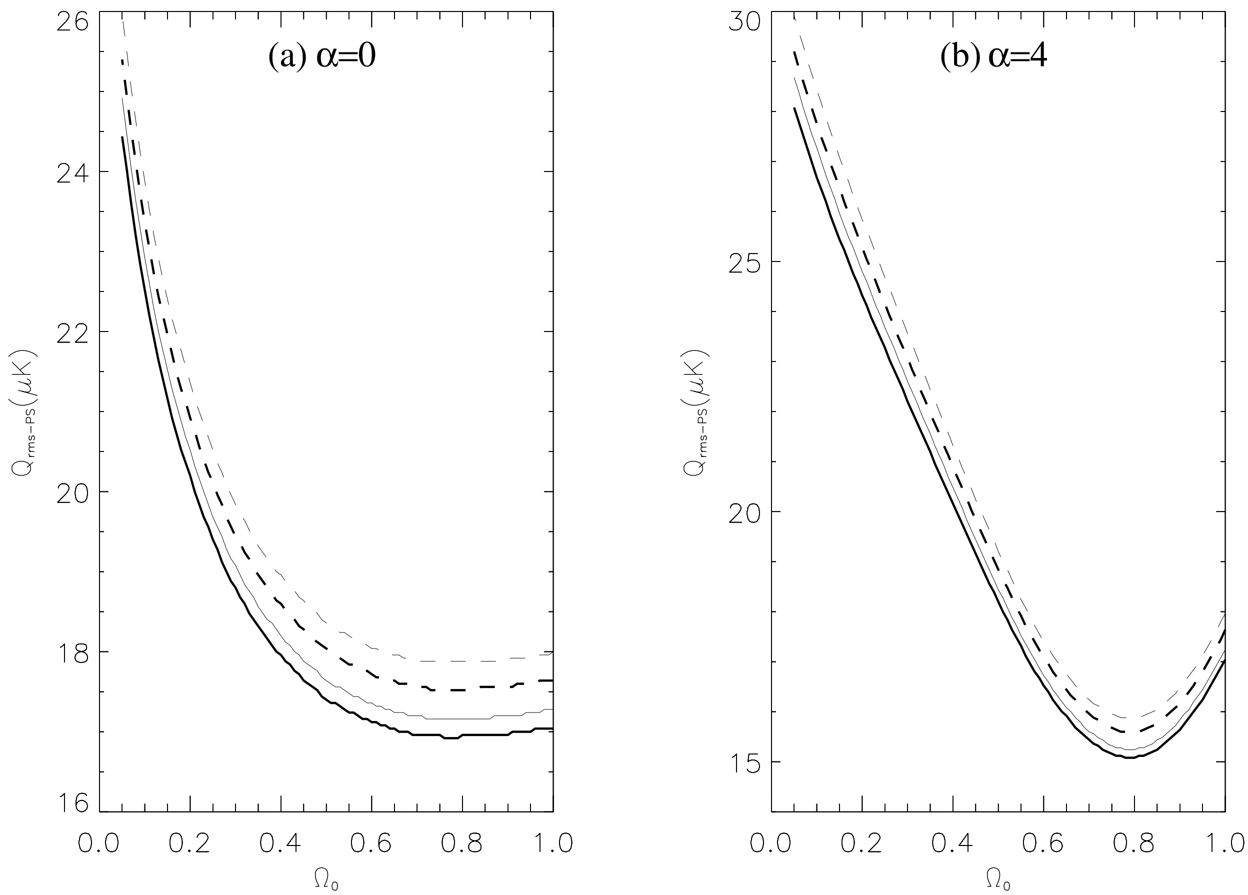

FIG. 5.—Ridge lines of the maximum likelihood $Q_{\text{rms-PS}}$ value as a function of Ω_0, for (*a*) $\alpha = 0$ and (*b*) $\alpha = 4$. These are for the model with $t_0 = 13$ Gyr and $\Omega_B h^2 = 0.014$. Four curves are shown in each panel: solid and dashed curves correspond to accounting for and ignoring the faint high-latitude foreground Galactic emission correction, respectively, while heavy and light curves correspond to including and excluding the quadrupole moment in the analysis, respectively.

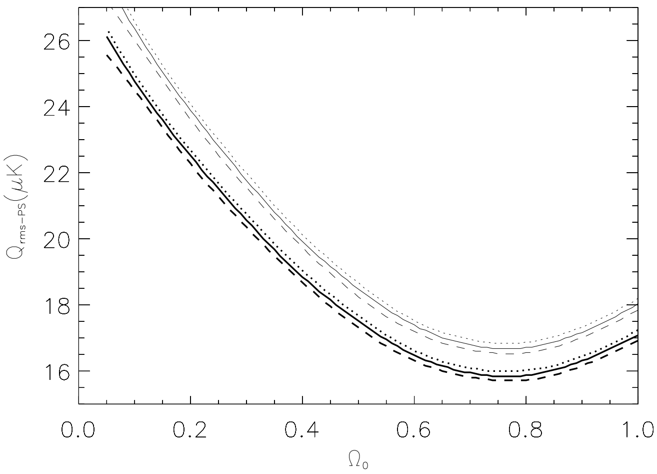

FIG. 6.—Ridge lines of the maximum likelihood $Q_{\text{rms-PS}}$ value as a function of Ω_0, for $\alpha = 2$. Six curves are shown. These correspond to parameter values $(t_0, \Omega_B h^2) = (11$ Gyr, 0.006) (*dotted curves*), (13 Gyr, 0.014) (*solid curves*), and (17 Gyr, 0.022) (*dashed curves*). Heavy curves are determined by accounting for faint high-latitude foreground Galactic emission and including the quadrupole moment in the analysis, while light curves ignore the correction for faint high-latitude foreground Galactic emission and exclude the quadrupole moment from the analysis.

TABLE 4

FRACTIONAL ENERGY-DENSITY PERTURBATION POWER SPECTRUM NORMALIZATION FACTOR Ah^4

	Ah^4 (10^5 Mpc^4)			
Ω_0 (1)	$\alpha = 0$ (2)	$\alpha = 2$ (3)	$\alpha = 4$ (4)	$\alpha = 6$ (5)
0.1	153 (28.4)	307 (47.0)	525 (69.1)	802 (92.9)
0.2	62.9 (14.6)	125 (23.2)	208 (33.1)	303 (42.9)
0.3	36.7 (9.82)	63.2 (14.1)	101 (19.3)	141 (24.2)
0.4	24.8 (7.28)	34.3 (9.14)	50.3 (11.7)	66.8 (14.1)
0.5	18.0 (5.64)	19.9 (6.14)	25.0 (7.16)	30.8 (8.13)
0.6	13.8 (4.48)	12.4 (4.31)	12.9 (4.49)	13.9 (4.69)
0.7	11.0 (3.62)	8.62 (3.21)	7.56 (3.01)	6.92 (2.87)
0.8	8.99 (2.96)	6.89 (2.59)	5.51 (2.30)	4.55 (2.06)
0.9	7.46 (2.45)	6.29 (2.24)	5.28 (2.05)	4.58 (1.88)
1	6.29 (2.05)	6.31 (2.05)	6.27 (2.05)	6.29 (2.05)

NOTES.—Normalized to the mean of the central $Q_{\text{rms-PS}}$ in the foreground-emission–corrected quadrupole-included and the foreground-emission–uncorrected quadrupole-excluded cases (normalized to $Q_{\text{rms-PS}} = 10\ \mu$K); scale as $(Q_{\text{rms-PS}})^2$. These are for the $t_0 = 13$ Gyr and $\Omega_B h^2 = 0.014$ models and are insensitive to the values of these parameters.

ranges between about 10% and 12%, depending on model parameter values, and the maximal 2 σ uncertainty ranges between about 16% and 19%. Since we have not done a complete analysis of all possible DMR data sets here, we adopt 10% and 20% as our 1 and 2 σ DMR-normalization uncertainties for the dark energy scalar-field models, for the purpose of comparing model predictions with observational measurements.

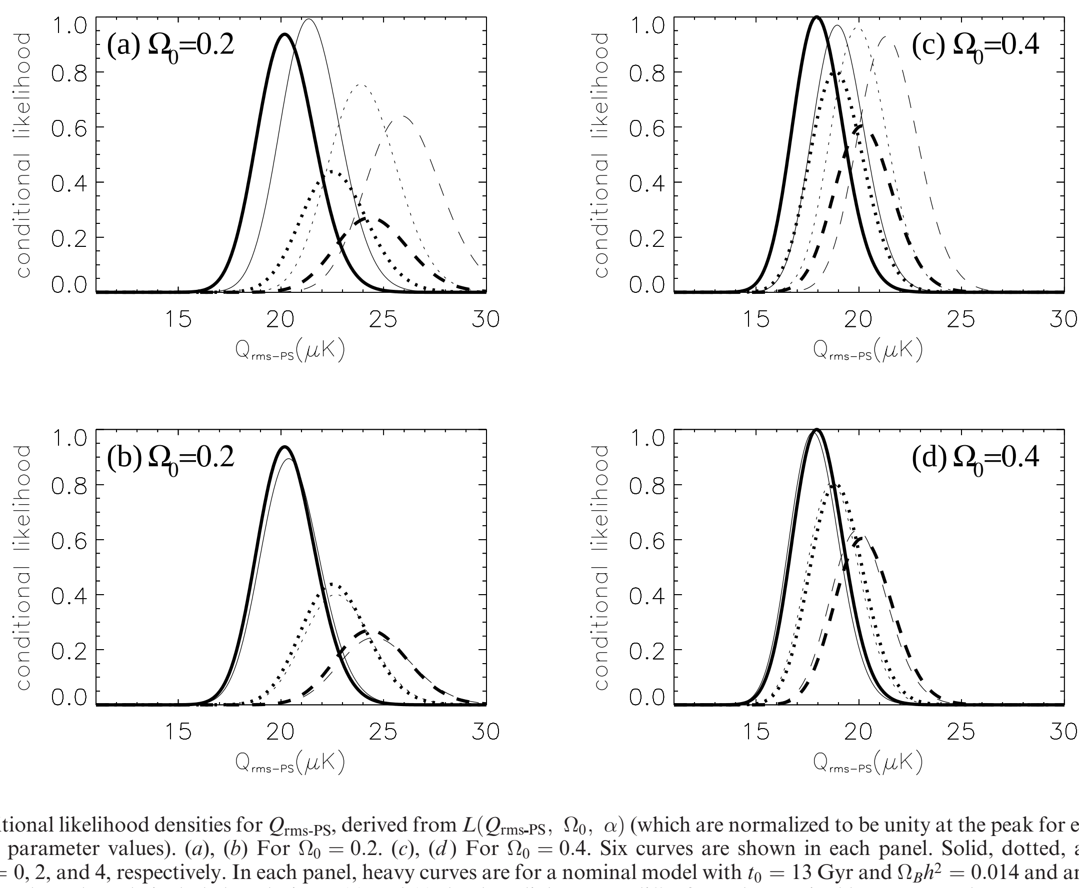

FIG. 7.—Conditional likelihood densities for $Q_{\text{rms-PS}}$, derived from $L(Q_{\text{rms-PS}}, \Omega_0, \alpha)$ (which are normalized to be unity at the peak for each DMR data set and set of model parameter values). (*a*), (*b*) For $\Omega_0 = 0.2$. (*c*), (*d*) For $\Omega_0 = 0.4$. Six curves are shown in each panel. Solid, dotted, and dashed curves correspond to $\alpha = 0$, 2, and 4, respectively. In each panel, heavy curves are for a nominal model with $t_0 = 13$ Gyr and $\Omega_B h^2 = 0.014$ and are derived from the foreground-corrected quadrupole-included analysis. In (*a*) and (*c*) the three light curves differ from the nominal heavy curves by not accounting for the faint high-latitude foreground Galactic emission correction and by excluding the quadrupole from the analysis. In (*b*) and (*d*) the three light curves differ from the nominal ones by corresponding to models with (*b*) $t_0 = 11$ Gyr and $\Omega_B h^2 = 0.006$ and with (*d*) $t_0 = 17$ Gyr and $\Omega_B h^2 = 0.022$.

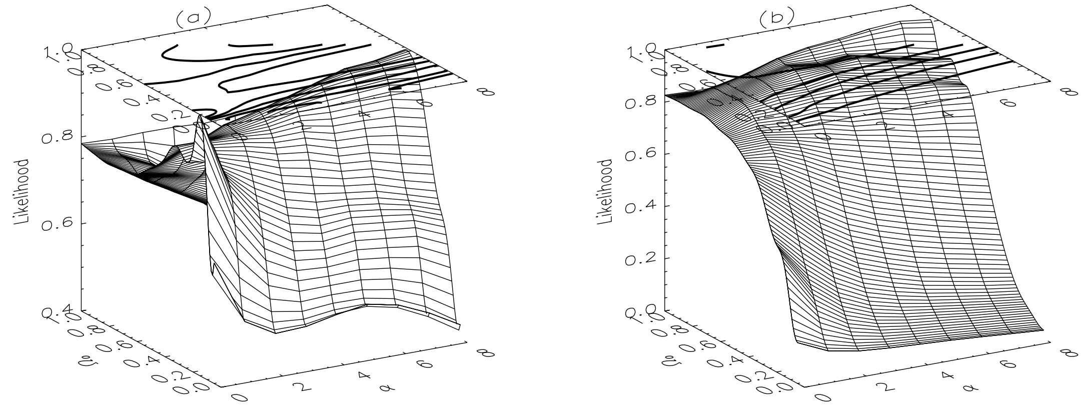

FIG. 8.—Likelihood functions $L(\alpha,\ \Omega_0)$ (arbitrarily normalized to unity at the highest peak) derived by marginalizing $L(Q_{\rm rms\text{-}PS},\ \alpha,\ \Omega_0)$ over $Q_{\rm rms\text{-}PS}$ with a uniform prior. These are for the model with $t_0 = 13$ Gyr and $\Omega_B h^2 = 0.014$. Panel *a* ignores the correction for faint high-latitude foreground Galactic emission and excludes the quadrupole moment from the analysis, while panel *b* corrects for faint high-latitude foreground Galactic emission and includes the quadrupole moment in the analysis.

4. OBSERVATIONAL CONSTRAINTS ON DMR-NORMALIZED MODELS

Given the dependence of the DMR likelihoods on the quadrupole moment of the CMB anisotropy, the DMR data do not meaningfully exclude any part of the (Ω_0, α, t_0, $\Omega_B h^2$) parameter space for the dark energy scalar-field model considered here. In this section we combine current observational constraints on cosmological parameters (as summarized in Peebles & Ratra 2003; Chen & Ratra 2003b; Bennett et al. 2003a) with the DMR-normalized model predictions to place semiquantitative constraints on the range of allowed model parameter values.

We focus on the parameter values and predictions of Tables 5–7. These are computed for parameter values $\Omega_B h^2 = 0.014$ and $t_0 = 13$ Gyr (Table 5), $\Omega_B h^2 = 0.006$ and

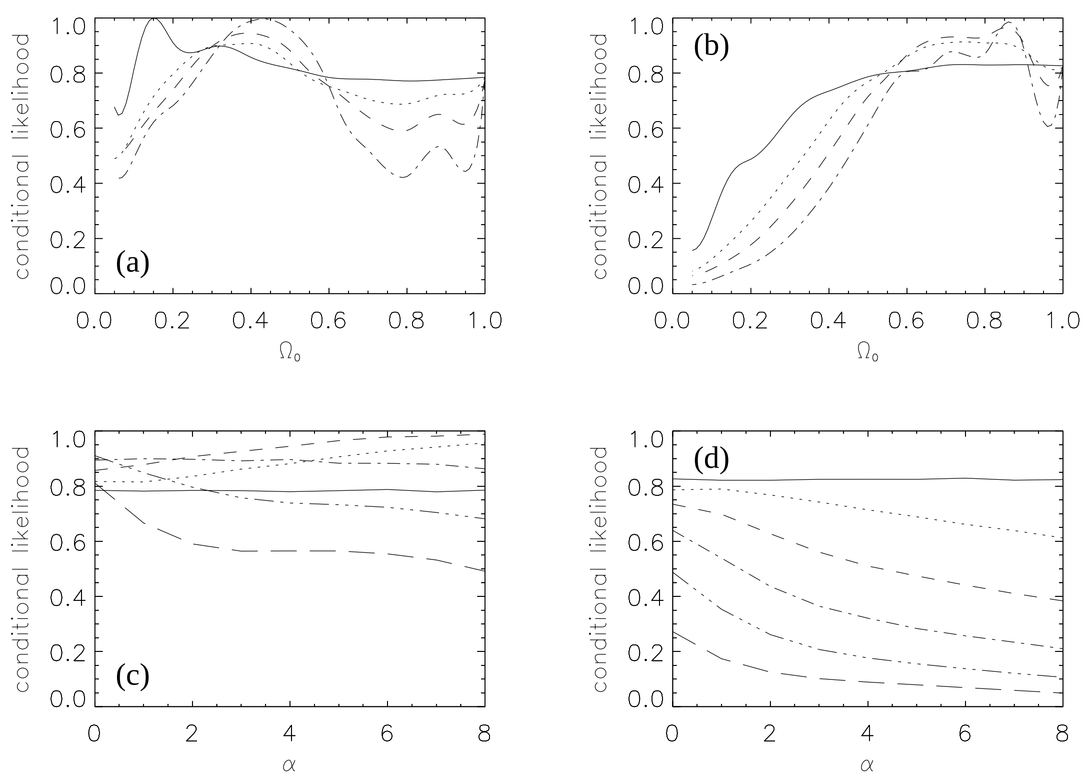

FIG. 9.—Conditional likelihood functions derived from $L(\alpha,\ \Omega_0)$ (arbitrarily normalized to unity at the highest peak), which is derived by marginalizing $L(Q_{\rm rms\text{-}PS},\ \alpha,\ \Omega_0)$ over $Q_{\rm rms\text{-}PS}$ with a uniform prior. These are for the model with $t_0 = 13$ Gyr and $\Omega_B h^2 = 0.014$. Panels *a* and *c* ignore the correction for faint high-latitude foreground Galactic emission and exclude the quadrupole moment from the analysis. Panels *b* and *d* account for the correction for faint high-latitude foreground Galactic emission and include the quadrupole moment in the analysis. (*a*), (*b*) Plot of $L(\Omega_0)$ on four constant-α slices at $\alpha = 0$ (*solid curves*), 2 (*dotted curves*), 4 (*dashed curves*), and 8 (*dot-dashed curves*). (*c*), (*d*) Plot of $L(\alpha)$ on six constant-Ω_0 slices at $\Omega_0 = 1$ (*solid curves*), 0.5 (*dotted curves*), 0.4 (*short-dashed curves*), 0.3 (*dot-dashed curves*), 0.2 (*triple-dot–dashed curves*), and 0.1 (*long-dashed curves*).

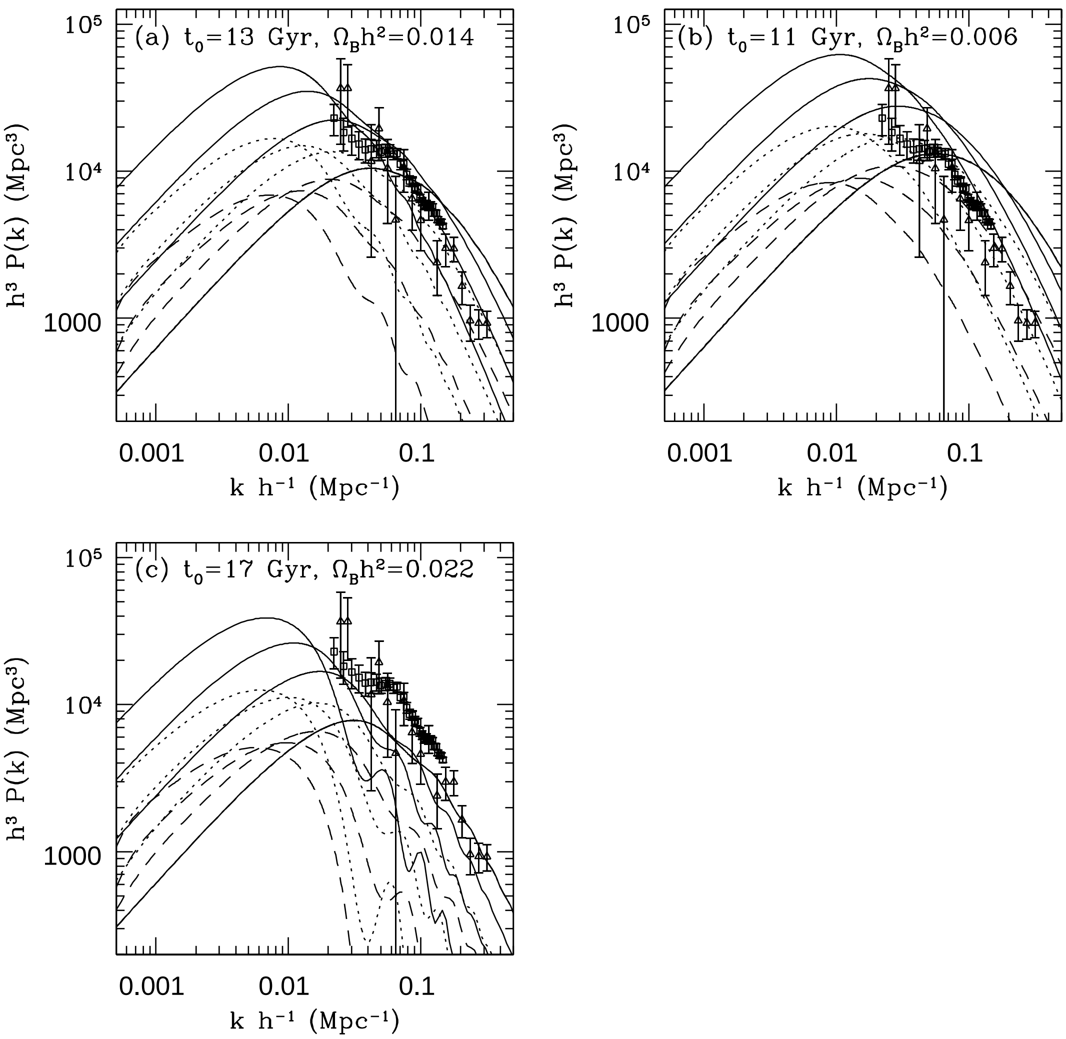

FIG. 10.—Fractional energy-density perturbation power spectra $P(k)$ as a function of wavenumber k. These are normalized to the mean of the central $Q_{\rm rms\text{-}PS}$ values from the foreground-corrected quadrupole-included analysis and the foreground-uncorrected quadrupole-excluded analysis (for the corresponding values of the cosmological parameters). Panels *a*, *b*, and *c* correspond to models with parameter values $(t_0,\ \Omega_B h^2) = (13\ \mathrm{Gyr},\ 0.014)$, (11 Gyr, 0.006), and (17 Gyr, 0.022), respectively. Each panel shows 12 power spectra at three values of $\alpha = 0$ (*solid curves*), 2 (*dotted curves*), and 4 (*dashed curves*) for four values of $\Omega_0 = 1$, 0.4, 0.2, and 0.1 in ascending order on the left axis of each panel. The triangles represent the linear real space power spectrum of the *IRAS* Point Source Catalogue Redshift Survey as estimated by Hamilton, Tegmark, & Padmanabhan (2000). Upper limits are not plotted. The squares represent the redshift-space galaxy power spectrum estimated from the Two-Degree Field Galaxy Redshift Survey optical galaxy data (Percival et al. 2001), again on linear scales, with comparison with the shapes of curves being valid in the case of linear bias.

$t_0 = 11$ Gyr (Table 6), and $\Omega_B h^2 = 0.022$ and $t_0 = 17$ Gyr (Table 7), which span the 2 σ range of interest:

$$11\ \mathrm{Gyr} \le t_0 \le 17\ \mathrm{Gyr}\ , \tag{6}$$

$$0.006 \le \Omega_B h^2 \le 0.022\ , \tag{7}$$

with central values of $t_0 = 13$ Gyr and $\Omega_B h^2 = 0.014$ (as summarized in Peebles & Ratra 2003; see Carretta et al. 2000, Krauss & Chaboyer 2001, and Chaboyer & Krauss 2002 for t_0, and Burles, Nollett, & Turner 2001 and Cyburt, Fields, & Olive 2001 for $\Omega_B h^2$). The recent *WMAP* measurements (Bennett et al. 2003a) lie in the center of the above t_0 range, 13.3 Gyr $\le t_0 \le$ 14.1 Gyr (2 σ), and near the upper end of the above $\Omega_B h^2$ range, $0.021 \le \Omega_B h^2 \le 0.024$ (2 σ), in good agreement with standard big bang nucleosynthesis theory and primordial deuterium abundance observations.

Column (1) in Tables 5–7 lists Ω_0. A recent analysis of pre-*WMAP* constraints on Ω_0 from a combination of dynamical, baryon fraction, power spectrum, weak lensing, and cluster abundance measurements results in the 2 σ range

$$0.2 \lesssim \Omega_0 \lesssim 0.35 \tag{8}$$

(Chen & Ratra 2003b), in striking accord with the Bennett et al. (2003a) *WMAP* estimate of $0.19 \le \Omega_0 \le 0.35$ (2 σ). This constraint on Ω_0 significantly narrows the range of viable model parameter values.

From an analysis of all available measurements of the Hubble parameter prior to mid-1999, Gott et al. (2001) find at 2 σ

$$0.6 \le h \le 0.74\ , \tag{9}$$

with central value $h = 0.67$. This is in good agreement with the *WMAP* estimate $0.65 \le h \le 0.79$ (2 σ), with central

TABLE 5
$(\delta M/M)(8\,h^{-1}\,\mathrm{Mpc})$ FOR THE $t_0 = 13$ Gyr, $\Omega_B h^2 = 0.014$ MODELS

Ω_0 (1)	h (2)	σ_8 $\alpha = 0$ (3)	$\alpha = 2$ (4)	$\alpha = 4$ (5)	$\alpha = 6$ (6)
0.1	0.96	0.632	0.295	0.169	0.107
0.2	0.81	0.888	0.509	0.332	0.234
0.3	0.72	1.02	0.670	0.479	0.363
0.4	0.67	1.10	0.798	0.617	0.495
0.5	0.62	1.14	0.906	0.745	0.633
0.6	0.59	1.17	0.991	0.863	0.771
0.7	0.56	1.18	1.06	0.972	0.905
0.8	0.54	1.18	1.11	1.06	1.02
0.9	0.52	1.18	1.15	1.12	1.11
1	0.50	1.17	1.17	1.17	1.17

NOTE.—The mean of the central values obtained from the foreground-emission–corrected quadrupole-included analysis and the foreground-emission–uncorrected quadrupole-excluded analysis.

TABLE 7
$(\delta M/M)(8\,h^{-1}\,\mathrm{Mpc})$ FOR THE $t_0 = 17$ Gyr, $\Omega_B h^2 = 0.022$ MODELS

Ω_0 (1)	h (2)	σ_8 $\alpha = 0$ (3)	$\alpha = 2$ (4)	$\alpha = 4$ (5)	$\alpha = 6$ (6)
0.1	0.73	0.273	0.107	0.0540	0.0316
0.2	0.62	0.453	0.241	0.149	0.101
0.3	0.55	0.562	0.352	0.244	0.179
0.4	0.51	0.631	0.445	0.336	0.265
0.5	0.48	0.675	0.523	0.425	0.356
0.6	0.45	0.707	0.589	0.509	0.450
0.7	0.43	0.724	0.645	0.588	0.544
0.8	0.41	0.740	0.689	0.655	0.629
0.9	0.40	0.748	0.725	0.709	0.698
1	0.38	0.751	0.751	0.750	0.751

NOTE.—The mean of the central values obtained from the foreground-emission–corrected quadrupole-included analysis and the foreground-emission–uncorrected quadrupole-excluded analysis.

value $h = 0.71$ (Bennett et al. 2003a). This constraint on h also significantly narrows the range of viable model parameters.

For an estimate of the rms linear fractional mass fluctuations at $8\,h^{-1}$ Mpc, we use, at $2\,\sigma$,

$$0.72 \leq \sigma_8 \leq 1.16\ , \tag{10}$$

with $\sigma_8 = 0.94$ as the central value (Chen & Ratra 2003b), with an additional $2\,\sigma$ DMR-normalization uncertainty of 20% added in quadrature.

Focusing on the numerical values of Tables 5–7 and combining the preceding constraints, there remains a small range of parameter space that is observationally viable. In particular, models with $\Omega_0 \sim 0.3$ and α ranging from 0 to $\sim$3, with $\Omega_B h^2 = 0.014$ and $t_0 = 13$ Gyr, are viable, while larger values of $\Omega_B h^2 = 0.022$ and $t_0 = 17$ Gyr narrow the range of α significantly, barely allowing a constant-Λ model with $\alpha = 0$. Dark energy models that deviate significantly from Einstein's cosmological constant are not favored by the data; i.e., the data favor α closer to 0. A model with $\alpha = 3$, as is still allowed, requires new physics near a characteristic energy scale of $\sim 10^3$ GeV (Peebles & Ratra 1988, 2003), which should soon be probed by accelerator-based elementary particle physics experiments.

TABLE 6
$(\delta M/M)(8\,h^{-1}\,\mathrm{Mpc})$ FOR THE $t_0 = 11$ Gyr, $\Omega_B h^2 = 0.006$ MODELS

Ω_0 (1)	h (2)	σ_8 $\alpha = 0$ (3)	$\alpha = 2$ (4)	$\alpha = 4$ (5)	$\alpha = 6$ (6)
0.1	1.13	0.964	0.477	0.283	0.185
0.2	0.96	1.26	0.746	0.498	0.356
0.3	0.86	1.41	0.945	0.685	0.522
0.4	0.79	1.49	1.10	0.854	0.689
0.5	0.74	1.52	1.22	1.01	0.862
0.6	0.70	1.54	1.31	1.15	1.03
0.7	0.66	1.54	1.39	1.28	1.19
0.8	0.64	1.53	1.44	1.38	1.33
0.9	0.61	1.51	1.47	1.44	1.44
1	0.59	1.49	1.49	1.49	1.49

NOTE.—The mean of the central values obtained from the foreground-emission–corrected quadrupole-included analysis and the foreground-emission–uncorrected quadrupole-excluded analysis.

5. CONCLUSION

We have normalized the inverse–power-law potential scalar-field dark energy model by comparing the predicted CMB anisotropy in this model with that measured by the DMR experiment. In addition to effects associated with the DMR data (see Górski et al. 1998 for a more detailed discussion), the model normalization is sensitive to the values of Ω_0 and α (the exponent of the inverse–power-law potential) but almost independent of the values of Ω_B and h.

The DMR data alone cannot be used to constrain Ω_0 and α over the ranges considered here. Current cosmographic observations, in conjunction with current large-scale structure observations compared with the predictions of the DMR-normalized dark energy scalar-field model, do, however, provide quite restrictive constraints on model parameter values. This is largely because σ_8 depends sensitively on the values of α and Ω_0 (see, e.g., Douspis et al. 2003), more so than the positions of the peaks in the CMB anisotropy spectrum.

As discussed in § 4, there is a small range of model parameter values in which evolving dark energy density models remain an observationally viable alternative to a constant cosmological constant model; however, the data do not favor large deviations from the constant-Λ model. It would therefore be of interest to examine more closely the supergravity-inspired generalization of the inverse–power-law potential scalar-field dark energy model (Brax & Martin 2000; Brax et al. 2000), which has a scalar-field potential that results in a slower evolution of the dark energy density, more like a constant Λ.

It is possible that current or future *WMAP* (see, e.g., Bennett et al. 2003a) and other CMB anisotropy data will significantly circumscribe this option (see, e.g., Baccigalupi et al. 2002; Mukherjee et al. 2003b; Caldwell & Doran

2003), although it should be noted that the constraints derived here are quite restrictive, since σ_8 is very sensitive to the values of α and Ω_0. Among other experiments, the proposed *Supernova/Acceleration Probe* space mission to measure the redshift-magnitude relation out to a redshift of 2 should also provide interesting constraints on evolving dark energy (see, e.g., Podariu, Nugent, & Ratra 2001a; Wang & Lovelace 2001; Weller & Albrecht 2002; Gerke & Efstathiou 2002; Eriksson & Amanullah 2002; Rhodes et al. 2003).

We acknowledge the advice and assistance of P. Brax, J. Lesgourgues, and J. Martin and thank the referee, M. Vogeley, for helpful comments. P. M. and B. R. acknowledge support from NSF CAREER grant AST 98-75031. This work was partially carried out at the Jet Propulsion Laboratory of the California Institute of Technology, under a contract with the National Aeronautics and Space Administration.

REFERENCES

Alam, U., Sahni, V., & Starobinsky, A. A. 2003, J. Cosmology Astropart. Phys., 4, 2
Baccigalupi, C., Balbi, A., Matarrese, S., Perrotta, F., & Vittorio, N. 2002, Phys. Rev. D, 65, 063520
Banday, A. J., Dickinson, C., Davies, R. D., Davis, R. J., & Górski, K. M. 2003, MNRAS, in press
Banday, A. J., et al. 1997, ApJ, 475, 393
Bennett, C. L., et al. 1996, ApJ, 464, L1
———. 2003a, ApJS, 148, 1
———. 2003b, ApJS, 148, 97
Boughn, S. P., & Crittenden, R. G. 2003, preprint (astro-ph/0305001)
Brax, P., & Martin, J. 2000, Phys. Rev. D, 61, 103502
Brax, P., Martin, J., & Riazuelo, A. 2000, Phys. Rev. D, 62, 103505
Burles, S., Nollett, K. M., & Turner, M. S. 2001, ApJ, 552, L1
Caldwell, R. R., & Doran, M. 2003, preprint (astro-ph/0305334)
Caldwell, R. R., Kamionkowski, M., & Weinberg, N. N. 2003, Phys. Rev. Lett., 91, 071301
Carretta, E., Gratton, R., Clementini, G., & Pecci, F. F. 2000, ApJ, 533, 215
Carroll, S. M., Hoffman, M., & Trodden, M. 2003, Phys. Rev. D, 68, 023509
Chaboyer, B., & Krauss, L. M. 2002, ApJ, 567, L45
Chae, K.-H., et al. 2002, Phys. Rev. Lett., 89, 151301
Chen, G., & Ratra, B. 2003a, ApJ, 582, 586
———. 2003b, PASP, 115, 1143
Cyburt, R. H., Fields, B. D., & Olive, K. A. 2001, NewA, 6, 215
Daly, R. A., & Djorgovski, S. G. 2003, ApJ, 597, 9
De Troia, G., et al. 2003, MNRAS, 343, 284
Douspis, M., Riazuelo, A., Zolnierowski, Y., & Blanchard, A. 2003, A&A, 405, 409
Durrer, R., Novosyadlyj, B., & Apunevych, S. 2003, ApJ, 583, 33
Dvali, G., & Turner, M. S. 2003, preprint (astro-ph/0301510)
Eriksson, M., & Amanullah, R. 2002, Phys. Rev. D, 66, 023530
Fischler, W., Ratra, B., & Susskind, L. 1985, Nucl. Phys. B, 259, 730
Fosalba, P., Gaztañaga, E., & Castander, F. 2003, ApJ, submitted (astro-ph/0307249)
Gerke, B., & Efstathiou, G. 2002, MNRAS, 335, 33
Górski, K. M. 1994, ApJ, 430, L85
Górski, K. M., Ratra, B., Stompor, R., Sugiyama, N., & Banday, A. J. 1998, ApJS, 114, 1
Górski, K. M., Ratra, B., Sugiyama, N., & Banday, A. J. 1995, ApJ, 444, L65
Górski, K. M., et al. 1996, ApJ, 464, L11
Gott, J. R. 1982, Nature, 295, 304
Gott, J. R., Vogeley, M. S., Podariu, S., & Ratra, B. 2001, ApJ, 549, 1
Hamilton, A. J. S., Tegmark, M., & Padmanabhan, N. 2000, MNRAS, 317, L23
Harrison, E. R. 1970, Phys. Rev. D, 1, 2726
Hauser, M. G., Kelsall, T., Leisawitz, D., & Weiland, J. 1998, *COBE* Diffuse Infrared Background Experiment (DIRBE) Explanatory Supplement (Greenbelt: NASA)
Hu, W., & Dodelson, S. 2002, ARA&A, 40, 171
Jain, D., Dev, A., & Alcaniz, J. S. 2003, Classical Quantum Gravity, 20, 4163
Kelsall, T., et al. 1998, ApJ, 508, 44
Klypin, A., Macciò, A. V., Mainini, R., & Bonometto, S. A. 2003, ApJ, submitted (astro-ph/0303304)
Komatsu, E., Wandelt, B. D., Spergel, D. N., Banday, A. J., & Górski, K. M. 2002, ApJ, 566, 19
Komatsu, E., et al. 2003, ApJS, 148, 119
Krauss, L. M., & Chaboyer, B. 2001, Nature, submitted (astro-ph/0111597)
Leibundgut, B. 2001, ARA&A, 39, 67
Melchiorri, A., & Ödman, C. J. 2003, Phys. Rev. D, 67, 081302
Mukherjee, P., Coble, K., Dragovan, M., Ganga, K., Kovac, J., Ratra, B., & Souradeep, T. 2003a, ApJ, 592, 692
Mukherjee, P., Dennison, B., Ratra, B., Simonetti, J. H., Ganga, K., & Hamilton, J.-C. 2002, ApJ, 579, 83
Mukherjee, P., Ganga, K., Ratra, B., Rocha, G., Souradeep, T., Sugiyama, N., & Górski, K. M. 2003b, Intl. J. Mod. Phys. A, in press
Mukherjee, P., Hobson, M. P., & Lasenby, A. N. 2000, MNRAS, 318, 1157
Munshi, D., Porciani, C., & Wang, Y. 2003, MNRAS, submitted (astro-ph/0302510)
Myers, A. D., Shanks, T., Outram, P. J., & Wolfendale, A. M. 2003, MNRAS, submitted (astro-ph/0306180)
Nolta, M. R., et al. 2003, ApJ, submitted (astro-ph/0305097)
Padmanabhan, T. 2003, Phys. Rep., 380, 235
Page, L., et al. 2003, ApJS, 148, 233
Park, C.-G., Park, C., Ratra, B., & Tegmark, M. 2001, ApJ, 556, 582
Peebles, P. J. E. 1984, ApJ, 284, 439
Peebles, P. J. E., & Ratra, B. 1988, ApJ, 325, L17
———. 2003, Rev. Mod. Phys., 75, 559
Peebles, P. J. E., & Yu, J. T. 1970, ApJ, 162, 815
Percival, W., et al. 2001, MNRAS, 327, 1297
Podariu, S., Daly, R. A., Mory, M. P., & Ratra, B. 2003, ApJ, 584, 577
Podariu, S., Nugent, P., & Ratra, B. 2001a, ApJ, 553, 39
Podariu, S., & Ratra, B. 2000, ApJ, 532, 109
Podariu, S., Souradeep, T., Gott, J. R., Ratra, B., & Vogeley, M. S. 2001b, ApJ, 559, 9
Ratra, B. 1985, Phys. Rev. D, 31, 1931
———. 1991, Phys. Rev. D, 43, 3802
Ratra, B., & Peebles, P. J. E. 1988, Phys. Rev. D, 37, 3406
———. 1995, Phys. Rev. D, 52, 1837
Ratra, B., & Quillen, A. 1992, MNRAS, 259, 738
Rhodes, J., et al. 2003, ApJ, submitted (astro-ph/0304417)
Rosati, F. 2003, Phys. Lett. B, 570, 5
Saini, T. D., Padmanabhan, T., & Bridle, S. 2003, MNRAS, 343, 533
Santos, M. G., et al. 2002, Phys. Rev. Lett., 88, 241302
Scranton, R., et al. 2003, Phys. Rev. Lett, submitted (astro-ph/0307335)
Sen, A., & Sen, S. 2003, Phys. Rev. D, 68, 023513
Silva, P. T., & Bertolami, O. 2003, ApJ, in press
Singh, P., Sami, M., & Dadhich, N. 2003, Phys. Rev. D, 68, 023522
Spergel, D. N., et al. 2003, ApJS, 148, 175
Tonry, J. L., et al. 2003, ApJ, 594, 1
Waga, I., & Frieman, J. A. 2000, Phys. Rev. D, 62, 043521
Wang, Y., & Lovelace, G. 2001, ApJ, 562, L115
Weller, J., & Albrecht, A. 2002, Phys. Rev. D, 65, 103512
Wetterich, C. 2003, Phys. Lett. B, 561, 10
Zel'dovich, Ya. B. 1972, MNRAS, 160, 1P
Zhu, Z.-H., & Fujimoto, M.-K. 2003, ApJ, 585, 52